SOURCE LOCALISATION AND JOINT VELOCITY MODEL BUILDING USING WAVEFRONT ATTRIBUTES

L. Diekmann, B. Schwarz, A. Bauer and D. Gajewski

email: *leon.diekmann@studium.uni-hamburg.de*

keywords: *passive seismic, localisation, wavefront attributes, tomography, inversion*

ABSTRACT

The localisation of passive seismic sources in form of microseismic tremors as well as large-scale earthquakes is a key issue in seismology. While most previous studies are assuming fairly good knowledge of the underlying velocity model, we propose an automatic spatial localisation and joint velocity model building scheme that is independent of detailed a priori information. The first step is a coherence analysis, estimating so-called wavefront attributes to locally describe the wavefield in terms of slopes and curvatures. In a similar fashion, we also obtain an initial guess of the source excitation times of the recorded events. The wavefront attributes constitute the input for wavefront tomography which represents the next step of the workflow and allows for a refinement of the previously evaluated source excitation times while simultaneously approximating the velocity distribution. In a last step, we use the final estimate of the velocity distribution and compute the respective image function by reverse time modelling to gain the source locations. This paper introduces the theoretical concept of our proposed approach for the general 3D case. We analyse the feasibility of our strategy and the influences of different acquisition settings by means of a synthetic 2D data example. The approach can deal with high levels of noise and low signal amplitudes, respectively, as well as sparse geophone sampling. The workflow generally delivers good approximations of the long-wavelength velocity variations along with accurate source locations.

INTRODUCTION

A passive seismic source can be defined as an origin of energy located within the interior of the Earth. Once, the energy is released at the source it propagates through the Earth and eventually reaches the surface, where the ground motion is recorded by seismic receivers. Such events occur on all scales, for instance in form of large-amplitude earthquakes or faint tremors which can hardly be felt by humans. Those weak events are referred to as microseismicity and can be induced either naturally or anthropogenically. Natural tremors occur for instance related to pressure fluctuations in volcanic (e.g. Aki et al., 1977) and geothermal areas. In the context of hydraulic fracturing, however, tremors are generated intentionally. By injecting a pressurised fluid into a wellbore, cracks arise in the rock formation, allowing for an improved flow of petroleum or gas when extracted. Monitoring aims at recording and localising these cracks to improve and control the fracturing processes (e.g. Maxwell and Urbancic, 2001). Independent of the triggering and scale of the events, the localisation of the sources is a key problem in seismology and fundamental for understanding both the physics behind the respective rupture processes and imaging the Earth's interior.

Of course there are many different approaches to deal with this issue. Most of them rely on a given velocity model and thus localise the sources in the assumed medium (e.g. Lomax et al., 2000). Some methods are based on picking traveltimes (e.g. Kennett and Engdahl, 1991; Waldhauser and Ellsworth, 2000). Such approaches, however, usually fail when the noise level is high and precise picking is hardly possible. Alternatively, the localisation can be performed by reverse time modelling (Gajewski and Tessmer, 2005) or diffraction stacking (e.g. Gajewski et al., 2007; Zhebel et al., 2011), back-projection (e.g. Ishii et al., 2005) and similar approaches (e.g. Grigoli et al., 2013). These methods can deal with high noise levels as they circumvent picking. Still, the respective results highly depend on the quality of the underlying velocity models. Recently, the increasing capacity of computational resources has paved the way for simultaneous approaches that invert for source locations and the velocity model at the same time. Wang and Alkhalifah (2018) have proposed a source function independent full waveform inversion (FWI) approach. In contrast to previous FWI-based methods (e.g. Sun et al., 2016) the need of a good starting guess of the velocity distribution has been relaxed by adopting a scheme which requires only a rough estimate of the vertical velocity variation. The method delivers accurate source locations and good velocity distributions. Nonetheless, the approach requires good data quality and generates high computational costs.

We propose an alternative, robust and efficient workflow to simultaneously estimate the velocity model and the source locations. The idea has initially been proposed by Schwarz et al. (2016) and exploits the fundamental robustness of coherence analysis. Stacking, forming a central ingredient of coherence analysis, has proven to be a reliable tool in controlled-source seismology and allows to access even weak events (e.g. Mayne, 1962; Taner and Koehler, 1969). Different traveltime operators have been proposed for coherence analysis over the years depending on different attributes (e.g. Landa et al., 2010; Schwarz et al., 2014). The common-reflection-surface method (Jäger et al., 2001) for instance delivers so-called wavefront attributes that describe the slopes and curvatures of the recorded wavefield. Apart from trace interpolation and data regularisation (Baykulov and Gajewski, 2009; Xie and Gajewski, 2017) these attributes can be used for wavefront tomography (Duveneck, 2004). The first step of our proposed method is to evaluate wavefront attributes for passive seismic data. Furthermore, we estimate the source excitation times of the recorded events by using an adapted traveltime operator. These source excitation times are then refined during wavefront tomography to eventually deliver a consistent velocity distribution. Finally, we use this velocity model for reverse time modelling to obtain an image function that localises the recorded energy sources.

WAVEFRONT ATTRIBUTES

The arrival time t of a passive seismic signal recorded at receiver location $\boldsymbol{x}$ can generally be expressed by

$$t(\boldsymbol{x}) = t_0(\boldsymbol{x}) + t_s \quad , \tag{1}$$

where t_0 is the actual traveltime from the source to the receiver and t_s marks the unknown source excitation time. In order to extract the event's kinematic information from the record, we want to use an analytic equation to approximatively represent the traveltime depending on the desired wavefront attributes. This can be achieved by means of a Taylor series expansion (e.g. Ursin, 1982; Castle, 1994). If we only consider receivers in the local vicinity of a given $\boldsymbol{x_0}$ according to

$$\boldsymbol{x} = \boldsymbol{x_0} + \boldsymbol{\Delta x} \quad , \quad \boldsymbol{x_0} = \begin{pmatrix} x_0 \\ y_0 \end{pmatrix} \quad , \quad \boldsymbol{\Delta x} = \begin{pmatrix} \Delta x \\ \Delta y \end{pmatrix} \quad , \tag{2}$$

where Δx and Δy are sufficiently small, the arrival time of the signal can be well approximated by the first-order Taylor series expansion about $\boldsymbol{x_0}$:

$$t(\boldsymbol{x}) \approx t(\boldsymbol{x_0}) + \boldsymbol{\nabla} t(\boldsymbol{x_0}) \cdot \boldsymbol{\Delta x} \tag{3}$$

$$\boldsymbol{\nabla} t = \begin{pmatrix} \frac{\partial t}{\partial x} & \frac{\partial t}{\partial y} \end{pmatrix} = \begin{pmatrix} \frac{\partial t_0}{\partial x} & \frac{\partial t_0}{\partial y} \end{pmatrix} \quad , \tag{4}$$

where $\boldsymbol{\nabla} t$ describes the gradient of t, which is similar to the gradient of t_0. Increasing the area of interest by regarding larger values of Δx and Δy, the second order term has to be taken into account:

$$t(\boldsymbol{x}) \approx t(\boldsymbol{x_0}) + \boldsymbol{\nabla} t(\boldsymbol{x_0}) \cdot \boldsymbol{\Delta x} + \frac{1}{2} \cdot \boldsymbol{\Delta x}^{\mathrm{T}} \cdot \underline{\mathbf{H}}(\boldsymbol{x_0}) \cdot \boldsymbol{\Delta x} \tag{5}$$

$$\underline{\mathbf{H}} = \begin{pmatrix} \frac{\partial^2 t}{\partial x^2} & \frac{\partial^2 t}{\partial x \partial y} \\ \frac{\partial^2 t}{\partial x \partial y} & \frac{\partial^2 t}{\partial y^2} \end{pmatrix} = \begin{pmatrix} \frac{\partial^2 t_0}{\partial x^2} & \frac{\partial^2 t_0}{\partial x \partial y} \\ \frac{\partial^2 t_0}{\partial x \partial y} & \frac{\partial^2 t_0}{\partial y^2} \end{pmatrix} \quad . \tag{6}$$

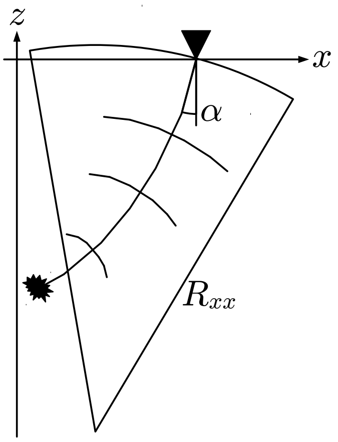

Figure 1: Sketch of source-receiver ray path along with wavefronts and the respective wavefront attributes α and R_{xx} in two dimensions. The quantity α marks the dip angle at the surface while R_{xx} equals the radius of the circle that locally fits the emerging wavefront in the best possible way.

The 2×2 matrix $\underline{\mathbf{H}}$ corresponds to the Hessian. In fact, the parabolic Equation 5 delivers a fairly good description of the moveout in the local vicinity of $\boldsymbol{x_0}$, however, in exploration seismology the hyperbolic expression, obtained from Equation 5 by subtracting t_s, squaring both sides and ignoring terms of third and higher order in $\boldsymbol{\Delta x}$, is usually preferred (e.g. Schleicher et al., 1993; Jäger et al., 2001):

$$t(\boldsymbol{x}) \approx \left\{ \left[t_0(\boldsymbol{x_0}) + \boldsymbol{\nabla} t(\boldsymbol{x_0}) \cdot \boldsymbol{\Delta x} \right]^2 + t_0(\boldsymbol{x_0}) \cdot \boldsymbol{\Delta x}^{\mathrm{T}} \cdot \underline{\mathbf{H}}(\boldsymbol{x_0}) \cdot \boldsymbol{\Delta x} \right\}^{\frac{1}{2}} + t_s \quad . \tag{7}$$

In case of a homogeneous velocity model this formula is actually exact. Both Equations 5 and 7 deliver accurate fits and contain the physically interesting quantities $\boldsymbol{\nabla} t$ and $\underline{\mathbf{H}}$. The gradient can be related to the horizontal slowness, composed of p_x and p_y, while the Hessian is linked to the curvature matrix $\underline{\mathbf{K}}$ (Hubral, 1983):

$$\boldsymbol{\nabla} t = \begin{pmatrix} p_x & p_y \end{pmatrix} = \begin{pmatrix} \frac{\sin(\alpha)\cdot\cos(\beta)}{v_0} & \frac{\sin(\alpha)\cdot\sin(\beta)}{v_0} \end{pmatrix} \tag{8}$$

$$\underline{\mathbf{H}} = \begin{pmatrix} H_{xx} & H_{xy} \\ H_{xy} & H_{yy} \end{pmatrix} = \frac{1}{v_0} \cdot \underline{\mathbf{L}} \cdot \underline{\mathbf{K}} \cdot \underline{\mathbf{L}}^{\mathrm{T}} \tag{9}$$

$$\underline{\mathbf{L}} = \begin{pmatrix} \cos(\alpha)\cdot\cos(\beta) & -\sin(\beta) \\ \cos(\alpha)\cdot\sin(\beta) & \cos(\beta) \end{pmatrix} \tag{10}$$

$$\underline{\mathbf{K}} = \begin{pmatrix} K_{xx} & K_{xy} \\ K_{xy} & K_{yy} \end{pmatrix} = \begin{pmatrix} 1/R_{xx} & 1/R_{xy} \\ 1/R_{xy} & 1/R_{yy} \end{pmatrix} \quad , \tag{11}$$

with α and β denoting the dip and azimuth angle, respectively, v_0 indicating the locally, meaning within the regarded surrounding of $\boldsymbol{x_0}$, constant near-surface velocity and K_{xx}, K_{xy} and K_{yy} representing the wavefront curvatures which are the reciprocals of the respective radii R_{xx}, R_{xy} and R_{yy}. Hence, there are five wavefront attributes: two angles and three curvatures. When considering only two dimensions, such that

$$\Delta y = 0 \quad , \quad \beta = 0 \quad , \quad K_{xy} = K_{yy} = 0 \quad , \tag{12}$$

Equation 5 simplifies to

$$t(x) \approx t(x_0) + \frac{\sin(\alpha)}{v_0} \cdot \Delta x + \frac{1}{2} \cdot \frac{\cos^2(\alpha)}{v_0 \cdot R_{xx}} \cdot \Delta x^2 \quad , \tag{13}$$

while Equation 7 becomes

$$t(x) \approx \left\{ \left[t_0(x_0) + \frac{\sin(\alpha)}{v_0} \cdot \Delta x \right]^2 + t_0(x_0) \cdot \frac{\cos^2(\alpha)}{v_0 \cdot R_{xx}} \cdot \Delta x^2 \right\}^{\frac{1}{2}} + t_s \quad . \tag{14}$$

The two remaining wavefront attributes α and R_{xx} are visualised in Figure 1.

The issue of estimating wavefront attributes for the recorded wavefield thus becomes an optimisation problem, where the coherent energy locally stacked along an analytical traveltime curve has to be maximised for each sample. The measure used to quantify coherence in this work is the normalised semblance coefficient (Taner and Koehler, 1969). We want to point out here that the parabolic Equation 5 is in fact a function of only the five wavefront attributes, whereas the hyperbolic Equation 7 additionally depends on the unknown source excitation time t_s.

In a first step, we can therefore estimate the wavefront attributes of the data using Equation 5. Because these attributes are local quantities of the wavefield the optimisation aperture used for this estimation should be as small as possible. This so-called optimisation aperture corresponds to the maximum $|\boldsymbol{\Delta x}|$ considered for the fitting process. An alternative to optimising the parabolic function for both first and second order attributes simultaneously is to find $\boldsymbol{\nabla} t$ via Equation 3 first (Mann et al., 1999). However, this requires a dense receiver sampling and high signal-to-noise ratio (SNR). As by-product, the obtained wavefront attributes can be used to enhance the recorded data by creating a stack, summing up all the samples along the analytically defined traveltime trajectories within a certain range around $\boldsymbol{x_0}$.

Afterwards, we use the wavefront attributes determined in the previous step and maximise the semblance using Equation 7 to approximate t_s. Since the source excitation time is constant for each event, we use the entire data ($\Delta x \to \infty$ and $\Delta y \to \infty$) in this second optimisation and compute the median of all estimates per event to obtain a final t_s value for each source. In this context, event tagging (e.g. Bauer et al., 2017a) is used to differentiate between signals from different sources.

Since the moveout might become fairly complex and t_s is simply approximated from the best hyperbolic fit, the results may vary in quality. It appears, however, that especially for moderate velocity variations the approach generally delivers a good initial guess of the source excitation times (Schwarz et al., 2016). In order to refine this guess and eventually be able to spatially localise the sources with a consistent velocity model, we use wavefront tomography.

WAVEFRONT TOMOGRAPHY AND IMAGE FUNCTION

Following coherence analysis each sample can be associated with a maximum semblance value as well as a set of wavefront attributes, kinematically describing the dominant local wavefield. Furthermore, all tagged samples which are thus regarded as signal rather than noise can be related to an initial source excitation time.

In order to get the input data $\boldsymbol{d}$ for wavefront tomography (Duveneck, 2004; Bauer et al., 2017b), the lateral coordinates $\boldsymbol{x}$, the traveltime τ, the horizontal slowness values $\boldsymbol{\nabla} t$ as well as the curvature related parameters $\underline{\mathbf{H}}$ are extracted automatically for samples exceeding a user-defined coherence threshold:

$$\boldsymbol{d}_i = (x, y, \tau, p_x, p_y, H_{xx}, H_{xy}, H_{yy})_i \quad , \quad i = 1, \ldots, n_{\text{data}} \quad , \tag{15}$$

with n_{data} denoting the total amount of picked data samples and $\boldsymbol{d}$ containing all $\boldsymbol{d}_i$. The picked time τ follows from correcting the measured time associated with the respective sample for the corresponding estimate of the source excitation time. Thus, it should ideally equal the source-receiver traveltime.

The model components $\boldsymbol{m}$ on the other hand comprise the velocity model

$$v_{jkl} \;,\; j = 1, \ldots, n_x \;,\; k = 1, \ldots, n_y \;,\; l = 1, \ldots, n_z \;, \tag{16}$$

defined in terms of B-splines (De Boor, 1978), with n_x, n_y and n_z marking the number of nodes used in x-, y- and z-direction, respectively, and

$$(x_0, y_0, z_0, e_x, e_y)_i \quad , \quad i = 1, \ldots, n_{\text{data}} \quad , \tag{17}$$

where $(x_0, y_0, z_0)_i$ gives the starting location of the upwards propagating ray corresponding to the ith data subset $\boldsymbol{d}_i$ and the horizontal components $(e_x, e_y)_i$ of the unit vector $\hat{\boldsymbol{e}}_i$ determine the ray emittance direction at this subsurface point. To obtain initial values for Expression 17, we assume an initial medium of constant near-surface velocity and use kinematic ray tracing to back propagate the picks $\boldsymbol{d}$ into the subsurface. Afterwards upward dynamic ray tracing can be performed to obtain the modelled data $\boldsymbol{d_{mod}}$ for the regarded model components $\boldsymbol{m}$.

Accounting for errors in the attribute estimation the inversion is implemented in a damped weighted least-squares sense (Tarantola, 2005). The objective function reads

$$S(\boldsymbol{m}) = \frac{1}{2}\Big\|\big(\boldsymbol{d} - \boldsymbol{d_{mod}}(\boldsymbol{m})\big) \cdot \boldsymbol{W}\Big\|_2^2 + \Lambda(v_{jkl}) \quad , \tag{18}$$

with $\boldsymbol{W}$ denoting the weighting vector that scales the different physical quantities and $\Lambda(v_{jkl})$ representing the regularisation term, favouring smooth velocity models. Minimising the objective function using the LSQR algorithm (Paige and Saunders, 1982) finally delivers a velocity model along with the corresponding ray starting points that is consistent with the input data $\boldsymbol{d}$. However, as the estimation of t_s via Equation 7 is approximative, the picked traveltimes τ occasionally tend to be quite erroneous and it might not always be possible to retrieve an appropriate estimate of the velocity distribution from the given input data. Getting good approximations of t_s intrinsically requires knowledge of the velocity model. Thus, we need to invert for both the velocity and the source excitation times simultaneously. Following a fairly pragmatic approach, we decouple the principal model space $\boldsymbol{m}$ and the source excitation times and simply minimise S as a function of the source excitation times, where the number of unknowns equals the number of tagged events. The starting guess of the respective t_s values is taken from the previous coherence analysis. In each iteration of the optimisation a certain constellation of source excitation times is fixed and the objective function is minimised depending on $\boldsymbol{m}$. The final value of S is then assigned to the tested set of source excitation times. If enough sources from a similar area contribute to the process, it leads to an effective refinement of the involved traveltimes.

Furthermore, the source excitation times with the overall minimal objective function value lead to a consistent velocity model. This model can be used for reverse time modelling (Gajewski and Tessmer, 2005). In the given examples we utilise the acoustic wave equation for constant density:

$$\nabla^2\psi = \frac{1}{V^2} \cdot \frac{\partial^2\psi}{\partial t^2} \quad , \tag{19}$$

where $\psi = \psi(x, y, z, t)$ is the pressure field and $V = V(x, y, z)$ denotes the acoustic velocity. Considering the time-reversed seismic data as surface boundary values, we model the wave propagation by finite differences until a predefined maximum time T is reached. The image function $f = f(x, y, z)$ resembles an energy and is given by

$$f = \int_0^T \psi^2 \, dt \quad . \tag{20}$$

The image function finally allows for a spatial, quasi-probabilistic localisation of the source energy by using the entire recorded wavefield depending only on the recovered velocity distribution but not on the estimated source excitation times.

NUMERICAL EXAMPLES

To test our proposed approach we first consider the optimal case of a densely sampled acquisition recording high-amplitude events. In order to show the benefits and underline the robustness of the method we subsequently show results for noise-contaminated and sparse data. For all three synthetic data examples we utilise the same velocity model and nine explosive sources, see Figure 2. The events are shifted by arbitrary source excitation times ranging from -1.50 s to 6.55 s. The datasets are simulated via finite-difference modelling, the recording time measures 10 s and the time sampling is 4 ms. The dominant frequency of the signals is about 10 Hz. Such a low frequency, however, is only chosen for visualisation purposes but not relevant for the success of the approach. Similarly, the workflow can be applied to all scales of events. Hence, it can equally deal with source depths of tens or even hundreds of kilometres if the acquisition surface is accordingly stretched.

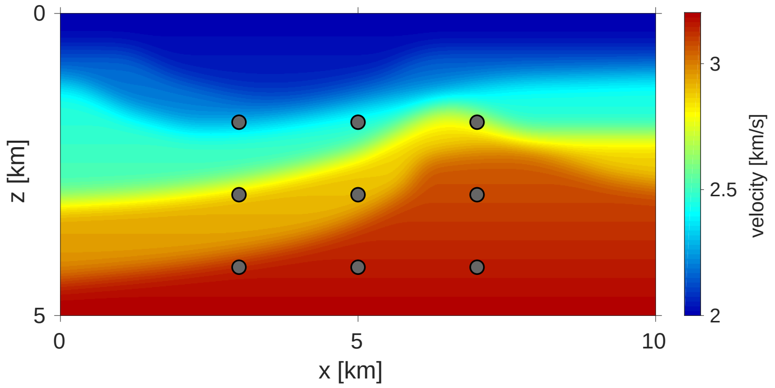

Figure 2: Velocity model and event locations (grey dots) for the synthetic data examples.

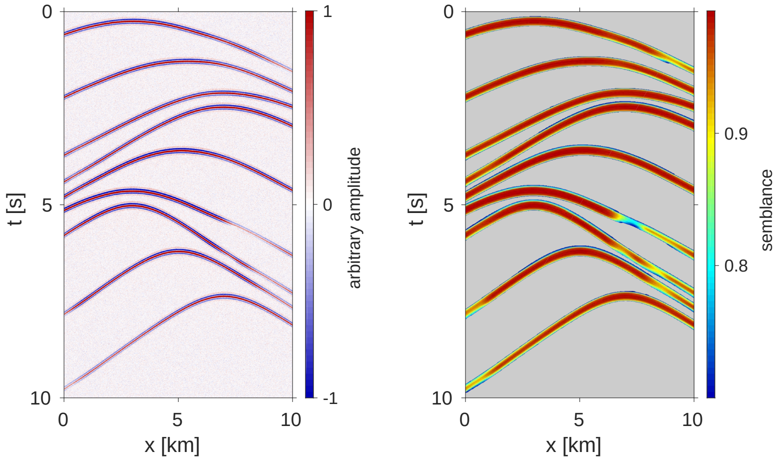

Figure 3: (left) Seismic surface recording for the first experiment. The colourbar is clipped at a half of the overall maximum amplitude. (right) Maximum semblance values obtained via the parabolic traveltime operator. Samples with a semblance value smaller than 0.7 are masked grey.

Proof of concept

For the first example we consider a total of 501 receivers which are equally distributed along the surface of the model in Figure 2, thus the receiver distance measures 20 m. We add Gaussian noise with a SNR of 20. The resulting seismic data are illustrated in Figure 3 (left).

Following our proposed workflow, we start by performing a local coherence analysis with the parabolic traveltime operator, Equation 5, to obtain wavefront attributes for the recorded wavefield. In this example, we use an optimisation aperture of 700 m. The coherence section, denoting the maximum semblance value for each sample, is shown in Figure 3 (right). The semblance values are apparently high along the nine events but low elsewhere. The resulting α and R_{xx} values are displayed in Figure 4 (top) and reveal smooth and physically reasonable variations.

As a next step, we fix these attributes and search for the optimal hyperbolic fit, Equation 7, for each sample of the data. Thereby, we obtain t_s as displayed in Figure 4 (bottom left). From a physical point of view, the source excitation time should be constant for each event. Since it is calculated using an analytical fitting operator, it seems obvious though that there might be variations along the events when laterally heterogeneous media are considered. While one can still assign a dominant colour and consequently a

tag	t_s^{true} [s]	t_s^{ini} [s]	t_s^{ref} [s]
1	-1.50	-0.60	-1.73
2	-0.40	-0.50	-0.58
3	0.50	1.15	0.36
4	1.25	1.25	1.09
5	2.30	2.25	2.14
6	3.30	3.75	3.15
7	4.15	4.20	4.08
8	5.35	5.30	5.26
9	6.55	6.45	6.46

Table 1: List of the true source excitation times t_s^{true}, the via parabolic fitting estimated values t_s^{ini} and the refined times t_s^{ref} for each tagged source.

source excitation time to each event, these t_s values may not necessarily be good approximations. In order to further investigate the quality of the estimated source excitation times, we tag the nine events. This can be done by evaluating the local wavefront resemblance (Bauer et al., 2017a) or, as there are no intersecting events in our example, simply by automatically labelling connected structures when ignoring samples with low coherence in the semblance section, compare Figure 3 (right). The tagging result is displayed in Figure 4 (bottom right). Thereby, we can assign the estimated source excitation times to the different events, analyse the arising deviations per source and compute median values to obtain a single t_s value for each tag. In Figure 5 we compare these results with the actual source excitation times. When considering the event-wise median values (dotted lines), the t_s approximations are in fact quite good in six of the overall nine cases. The three erroneous source excitation times, however, differ from the true values by up to 0.9 s. This leads to significantly biased input data for wavefront tomography.

Therefore, we need to refine the source excitation times. The tag-wise median values of the previously estimated source excitation times constitute our initial guess for wavefront tomography. As previously explained, the space of unknowns is split into the source excitation times and the standard model space $\boldsymbol{m}$. We have tested different optimisation algorithms in the context of refining the t_s values and decided to minimise the objective function with a pattern search algorithm (Hooke and Jeeves, 1961). This eventually leads to refined t_s values for the nine events. In Table 1 we compare the true, initial and refined source excitation times. We observe that the large errors of events 1, 3 and 6 are reduced significantly and all nine source excitation times are sufficiently well approximated. However, all refined source excitation times are underestimating their true values by about 0.1 s to 0.2 s. This might for instance be due to the node spacing, the regularisation and weighting factors or the initial velocity distribution and will be further investigated in the future.

Finally, we can also examine the respective velocity distribution and ray starting locations. Using the refined source excitation times the initial guess of the parameters $\boldsymbol{m}$ is illustrated in Figure 6 (top). The velocity distribution is homogeneous with value v_0 and the corresponding ray starting locations follow from downward kinematic ray tracing. The final model is displayed in Figure 6 (middle). One can easily recognise some of the underlying velocity features, as for instance the low-velocity moat in the shallower left part and the deeper rightwards rising high-velocity layer. Additionally, the final ray starting points clearly cluster in nine distinct regions close to the true source locations. These clusters, however, are all slightly too deep. This is a result of the generally underestimated source excitation times. When evaluating the relative velocity error, Figure 6 (bottom), we denote a maximum absolute value of nearly $12\ \%$. This error is due to the underestimation of the velocities in particular at the top of the fast layers. The general underestimation of velocities is probably also a result of the underestimated source excitation times. Still, the long-wavelength velocity structure is resolved quite successfully. Obviously, only those regions of the model that have been traversed by rays contain reliable velocity information. In this sense, the bottom left and bottom right part of the model result from the regularisation.

Lastly, we can use the recovered velocities to perform reverse time modelling. In so doing we localise the energy sources of the recorded wavefield in a more probabilistic and continuous manner. The resulting

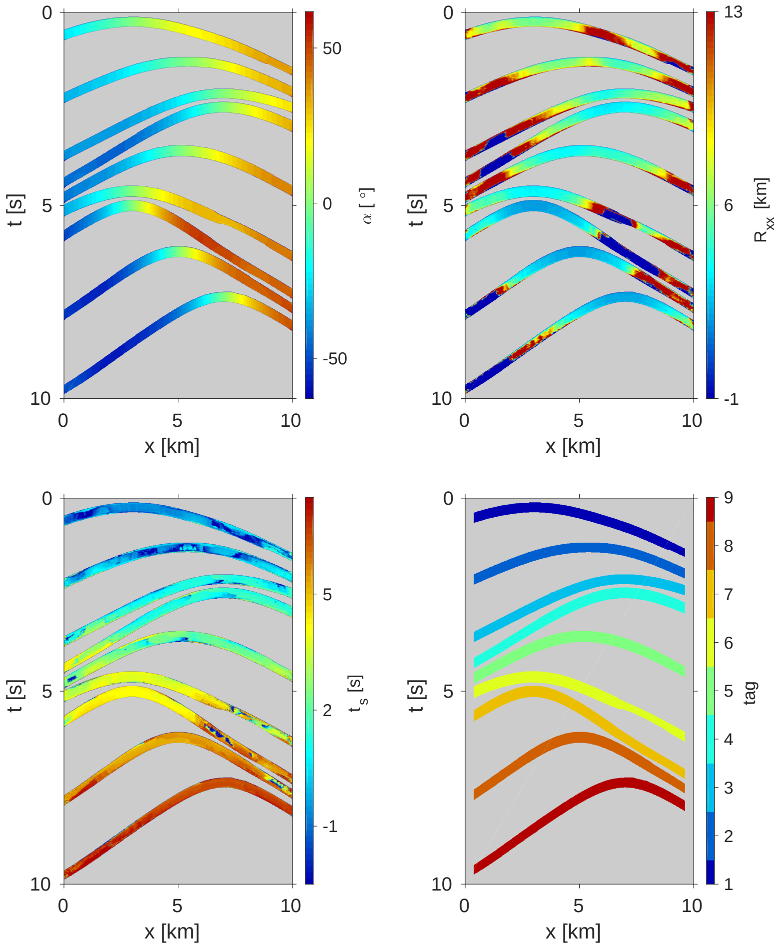

Figure 4: Visualisation of wavefront attributes α (top left) and R_{xx} (top right) as well as sample-wise source excitation times t_s (bottom left). Contributions from samples with low coherence are masked grey. The R_{xx} values are clipped at -1 km and 13 km, respectively. (bottom right) Tagging result. The boundaries of the acquisition are muted prior to the labelling procedure to account for possible boundary effects in the coherence estimation.

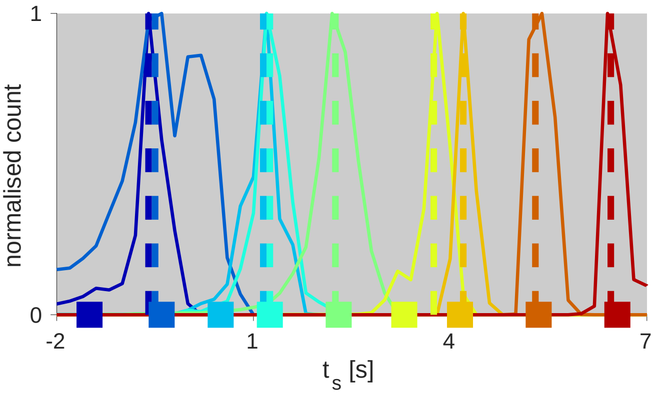

Figure 5: The nine colours match the tag numbers in Figure 4 (bottom right). The centres of the squares at the bottom of the plot mark the actual source excitation times. The continuous lines sketch the normalised counts of all estimated t_s values per event and therefore resemble histograms. Contributions from samples that are assigned low coherence during the hyperbolic fitting process are ignored. The dashed lines denote the resulting median values.

image function can be seen in Figure 7. It reveals nine distinct regions of relatively high energy that nicely coincide with the actual source locations, generally deviating by less than the dominant wavelength of the signal.

These results confirm the general functionality of our proposed method. Assuming knowledge of only the locally constant near-surface velocity, we are able to approximate the coarse velocity distribution and localise the sources in the subsurface. The following examples further examine the method by considering the influences of noise and sparse spatial sampling.

Noisy data

The dataset for this example equals the previous one except for the SNR which is set to 0.5. The corresponding data are displayed in Figure 8 (left). Due to the high noise level and low signal amplitudes, respectively, the nine events are poorly visible.

Because of the intrinsic robustness of coherence analysis we can nonetheless estimate wavefront attributes for the data. In order to reach significant coherence levels that allow to distinguish signal from noise, the optimisation aperture has to be sufficiently wide. We choose an optimisation aperture of 1000 m for the hyperbolic traveltime fitting. As already mentioned, the wavefront attributes do not only enable wavefront tomography, but also allow for data enhancement by stacking. This can be comprehended in Figure 8 (right). The previously invisible events are now fairly distinct. The signal only remains noisy in areas of particularly low amplitudes, straight slopes and in the vicinity of the acquisition boundaries, hence, wherever the attribute estimation is particularly difficult.

Estimating t_s values and tagging the events allows for evaluating a median source excitation time for each tagged source. Refining these times during the inversion leads to the final model parameters in Figure 9 (top). Again, having started from a constant near-surface velocity medium, the final velocity distribution maps the main features of the model, although it might seem less accurate in some areas compared to Figure 6 (middle). Furthermore, the focusing of the ray starting locations appears slightly worse and reveals distinct offsets compared to the true source locations, especially for the two events localised at the bottom left and bottom right of the model. The relative error of the velocities is shown in Figure 9 (middle). The erroneous underestimated area in the centre seems to be slightly extended in space. The maximum absolute value of the relative error measures more than 13 % and is thus marginally higher than in the previous experiment. Altogether, the overburden structure is in fact similarly resolved - despite the poor data quality.

Figure 9 (bottom) shows the corresponding image function. Due to the still relatively high noise level in the stack, the background noise of the image function is high. Nevertheless, most of the energy gets focused

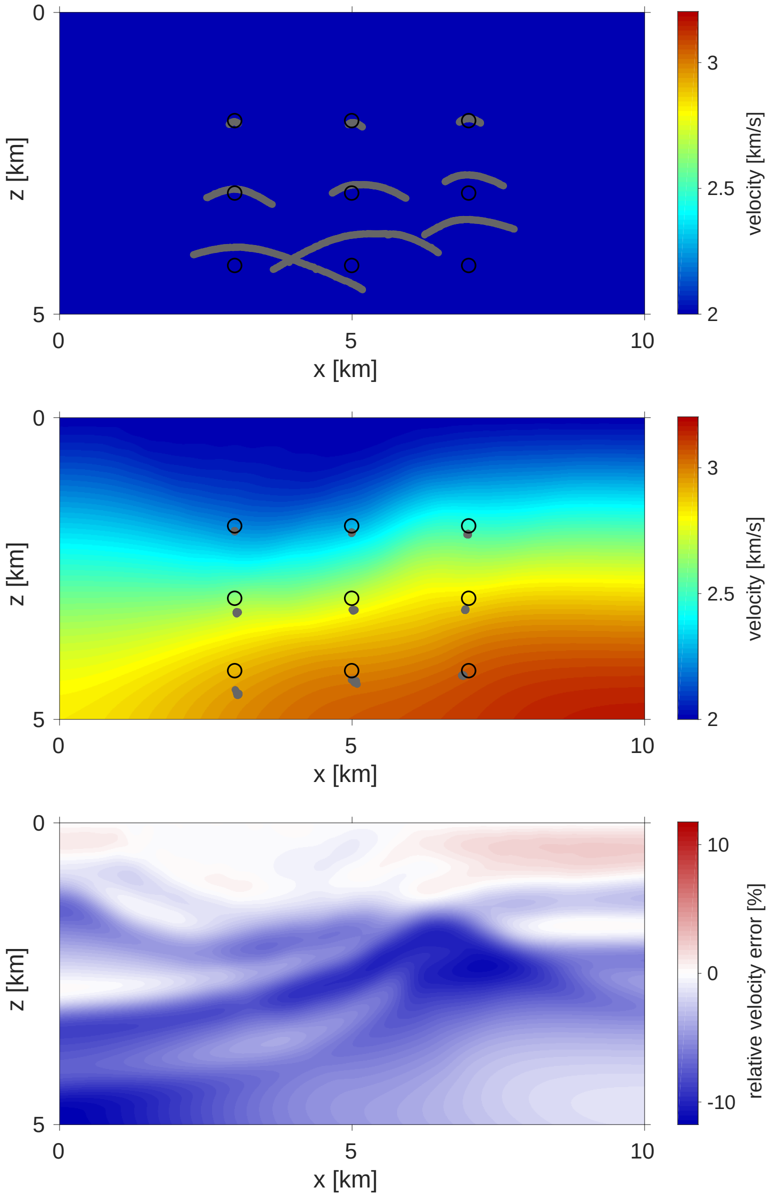

Figure 6: (top) Initial model. (middle) Final model. The grey dots mark the ray starting locations for the respective velocity models, the black circles show the actual source positions. The colourbars are clipped at the minimum and maximum velocity values of the true model. (bottom) Relative velocity error.

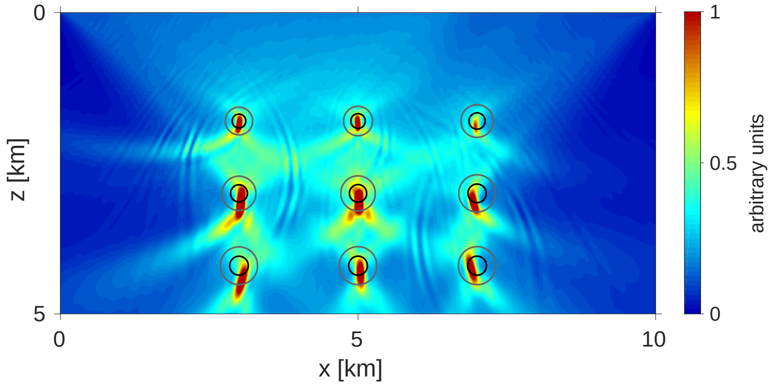

Figure 7: Image function obtained from reverse time modelling for the estimated velocity distribution in Figure 6 (middle). The colourbar is clipped at $40\ \%$ of the maximum energy. The circles are centred at the true source locations. Black circles have a radius of half, grey circles of once the dominant signal wavelength.

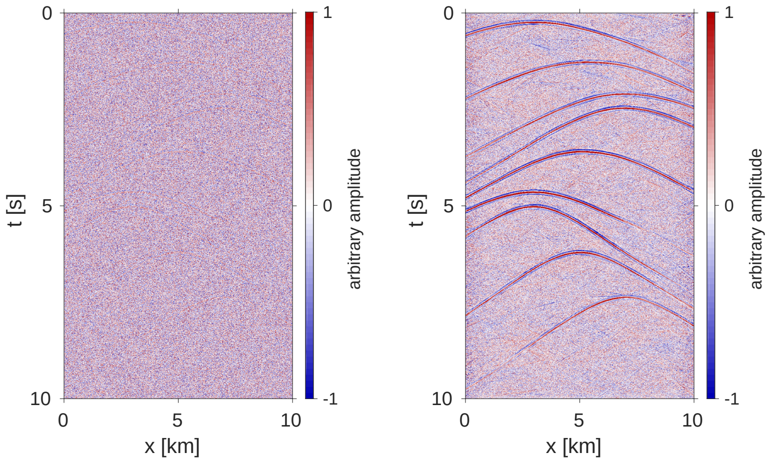

Figure 8: (left) Seismic surface data with an SNR of 0.5. (right) Enhanced dataset, obtained from stacking according to the estimated wavefront attributes α and R_{xx}. The stacking aperture measures 700 m, hence 71 receivers contribute to each stacked trace. Both colourbars are clipped at a half of the respective overall maximum amplitude.

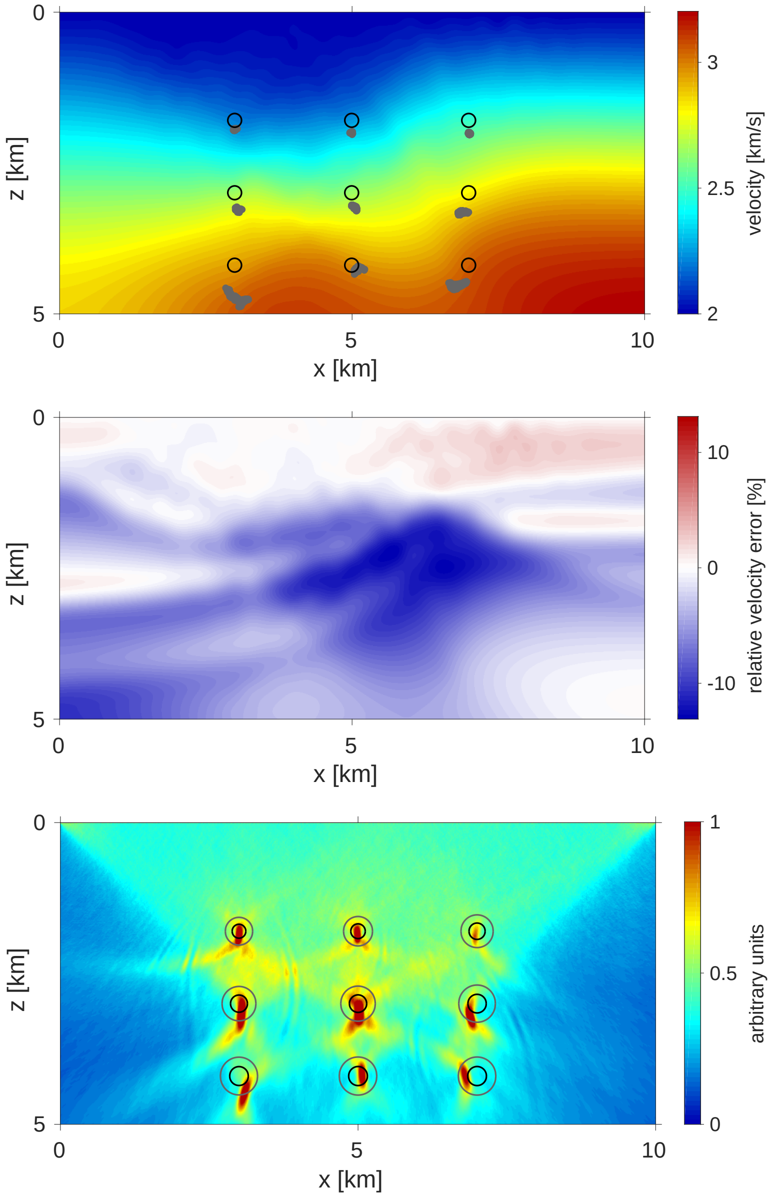

Figure 9: (top) Final tomographic velocity model for the noisy dataset. The grey dots mark the final ray starting locations, the black circles show the actual source positions. The colourbar is clipped at the minimum and maximum velocity values of the true model. (middle) Relative velocity error. (bottom) Image function obtained from reverse time modelling. We have used the enhanced data, Figure 8 (right), since the image function of the original data has been heavily contaminated by noise. The colourbar is clipped at 21 % of the maximum energy. The circles are centred at the true source locations. Black circles have a radius of half, grey circles of once the dominant signal wavelength.

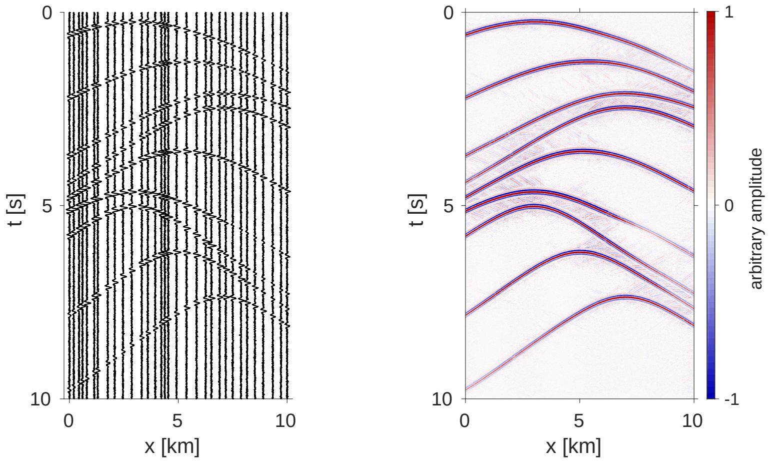

Figure 10: (left) Seismogram using a random selection of only 32 stations. (right) Enhanced and regularised data, obtained from stacking according to the estimated wavefront attributes α and R_{xx}. The stacking aperture measures 700 m. In order to reduce spatial aliasing artefacts the stack has been weighted with the smoothed semblance section. The colourbar is clipped at a half of the overall maximum amplitude.

in nine distinct regions, generally close to the true source locations. As a matter of fact, these peaks seem to be located slightly better than the final ray starting locations in Figure 9 (top). This is due to the fact that for the ray tracing both the erroneous velocities and the erroneous traveltimes are implicated, while for the reverse time modelling only the velocities matter. Only the leftmost event exhibits a slightly larger error in the image function, however, it is still within once the dominant wavelength.

Considering that we have only used the data in Figure 8 (left) and exploited no other a priori information than the near-surface velocity, these results are surprisingly good. However, such noisy acquisition environments implicate a trade-off between increasing the optimisation aperture to detect signals during the coherence analysis and keeping it small to enable a local wavefront attribute estimation and thus obtain high quality input data for the inversion. The suggested approach is generally applicable independent of high noise levels and low signal amplitudes, respectively, but might decrease in quality with decreasing SNR.

Sparse data

Finally, we want to analyse the influence of sparse data sampling. Therefore, we use a random selection of 32 from the previously used 501 receivers. The geophone distances vary from 160 m to 460 m. We add Gaussian noise with a SNR of 10. The seismic data are visualised in Figure 10 (left).

As a matter of fact, the estimation of wavefront attributes not only allows for increasing the SNR, it also enables data interpolation. This can easily be achieved by estimating the wavefront attributes for all lateral positions that one wants to interpolate the data at. Having those attributes, one can simply create a stack to locally interpolate the recorded wavefield. We use an optimisation aperture of 1000 m to estimate α and R_{xx} and create an interpolated stack, see Figure 10 (right). While the stacked seismogram reveals some minor artefacts due to spatial aliasing (compare the high-amplitude slanting stripes especially at the left-hand side at about 5 s), the events are still nicely interpolated. After all, such aliasing can easily be further suppressed, for instance by a more constrained attribute estimation. Considering the reverse time modelling this denser data should allow for a smoother image function displaying less imaging artefacts than the original data.

As before, the source excitation times are estimated and tag-wise refined to eventually also deliver a consistent inversion result starting again from a constant near-surface velocity medium. The final velocity distribution is shown in Figure 11 (top). The recovered velocities are quite similar to the two previous results, while the focusing of the ray starting locations is marginally better than for the noisy dataset. However, the positions of the nine clustering regions are again slightly to deep, in particular considering the deepest, leftmost event. The relative velocity error, Figure 11 (middle), is similar in shape and magnitude to the one for the first dataset. Thus, the maximum absolute value measures approximately 12 %, but the absolute values on average range from 4 % to 5 %.

Finally, we use the interpolated seismic section, Figure 10 (right), along with the estimated velocity distribution and perform reverse time modelling. In fact, the image function, Figure 11 (bottom), looks very similar to the one in Figure 7. In general, the nine energy peaks coincide nicely with the true source locations. Some of the maxima, however, appear to some extend blurred and slightly worse located, but overall the method delivers good results.

Even from such a sparse acquisition with only 32 stations along a 10 km profile we can still get a sufficiently accurate approximation of the velocity model and thereby localise the sources via reverse time modelling. We do not need detailed a priori information and perform data interpolation on the fly. Sparser sampling or larger data gaps would require a larger optimisation aperture and thereby decrease the quality of the wavefront attributes. Nonetheless, the workflow can generally deal with sparse acquisitions.

DISCUSSION

Using wavefront attributes of passive seismic data we have presented a workflow for simultaneous localisation and velocity model building. The method needs basically no a priori information. However, we have assumed to know the locally constant near-surface velocity for the presented examples, where local corresponds to the extend of the optimisation aperture. In general, even a rough estimate of the average velocity of the upper layers should constitute an adequate starting guess. The wavefront attribute estimation and the inversion are carried out in an automatic manner, where the optimisation apertures in the coherence analysis and the regularisation and weighting factors as well as the node spacing in the tomography have to be adjusted empirically. No time-consuming user interaction, as for instance manual picking, is required.

In order to use the method successfully, the quality of the estimated wavefront attributes is crucial. Ideally, the apex areas of the events of interest are covered by a sufficiently dense acquisition to enable a reliable attribute estimation, particularly considering wavefront curvatures. As apex area we refer to a circular surface with a radius of roughly the source depth centred at the epicentre. The curvature of the wavefront is significantly different from zero there and can be sufficiently well estimated for wavefront tomography. Generally speaking, it is necessary that the receiver array records curved wavefronts. In that sense, the epicentres might also be located beyond the acquisition surface, however, they should not be arbitrarily far away. As already discussed previously, it is hard to determine what exactly marks an acquisition to be sufficiently dense. One could probably further reduce the number of receivers in example I to about 20 and the approach would still work. However, that would probably require larger optimisation apertures and thus provide a less local estimation of the wavefront attributes, increasing the potential to average possible lateral variations. As a result one might obtain a smoother, less accurate velocity distribution. The similar trade-off is present for noisy data. Increasing the optimisation aperture might be necessary to distinguish signals from noise and get wavefront attributes at all but this may also decrease the quality of the estimated wavefront attributes.

If a refinement of the source excitation times is desired, multiple events from a similar region are necessary to ensure that a simultaneous inversion for improving the source excitation times and approximating the velocity distribution is successful. From our experience this approach leads to considerable improvements, especially regarding large errors in the initial source excitation times, see Table 1.

If these conditions are fulfilled, our workflow is a promising tool to localise passive seismic sources and simultaneously estimate the previously unknown subsurface velocities. Because of its built-in regularisation and data enhancement facility it is quite robust and can deal with high noise levels and low-amplitude signals, respectively, as well as sparse data acquisitions. In our examples, the velocity distributions are approximated with a mean relative error of about 4 % considering absolute values. The sources, on the other hand, are localised with a maximum deviation in the order of the dominant wavelength of the signals. We have also exploited the potential of reverse time modelling, which does not dependent on errors in the source excitation time estimation. Thus, the sources are localised more accurately by reverse modelling than by wavefront tomography.

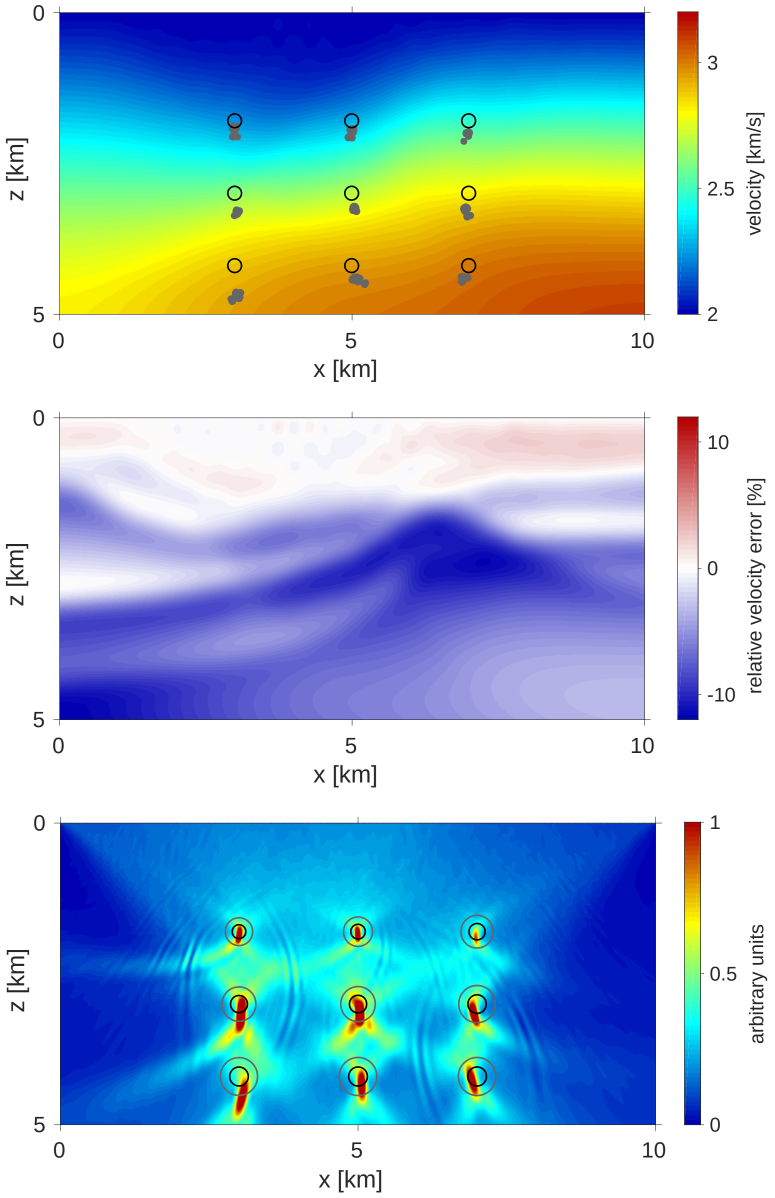

Figure 11: (top) Final tomographic model. The grey dots mark the ray starting locations, the black circles show the actual source positions. The colourbar is clipped at the minimum and maximum velocity values of the true model. (middle) Relative velocity error. (bottom) Image function obtained from reverse time modelling. We have used the enhanced and regularised data, Figure 10 (right), instead of the original data. The colourbar is clipped at $40\ \%$ of the maximum energy. The circles are centred at the true source locations. Black circles have a radius of half, grey circles of once the dominant signal wavelength.

In order to further improve the results of the suggested approach, one could create a recursive scheme building on our workflow. The next step would involve an update of the source excitation times based on the improved source locations determined by reverse time modelling. Exploiting those new source excitation times another tomographic inversion to improve the velocity distribution could be carried out, followed by reverse time modelling to update the source locations again. Linking the two steps in such an iterative process combines the robustness of kinematic tomography and the independence of wavefield modelling from the tomography's possibly erroneous input picks. In terms of computation, other optimisation techniques might be investigated to improve and speed up the refinement of the source excitation times. Alternative curvature-based inversion schemes such as geometrical spreading focusing (Znak et al., 2018) could be investigated to further promote the workflow. Adapting the wavefront inversion concept to the characteristics of passive sources and including the tagging attribute (Bauer et al., 2017a) as additional information may further improve the inversion process. Knowing that equally tagged picks should focus in the respective hypocentre allows for reducing the model space and testing alternative objective functions. In fact, this feature of passive seismic events is equally interesting for diffractions in active seismic experiments (Bauer et al., 2017b).

The presented synthetic data examples are considered here for demonstration purposes. Localisation is an inherently three-dimensional problem. The theoretical background of our approach has already been presented for 3D media and the extension of the computer codes to 3D is straight forward. A more involved issue might be to handle complicated source mechanisms. The approach obviously works best for explosive sources, however this is not a restriction. In general it is sufficient, if the waveforms are consistent within the optimisation area. For instance, one could perform coherence analysis for the envelope of the seismic wavefield to resolve source radiation issues. Future work might also consider extended sources. A potential improvement of the inversion results might be obtained by including other phases, like S-waves. Since they have the same source excitation times as the respective P-waves and larger moveouts, that is larger curvatures, they might benefit the source excitation time estimation. Apart from that, the slight, but systematic underestimation of source excitation times is an issue which certainly needs further investigations.

CONCLUSION

We have presented a workflow to simultaneously determine source locations and seismic velocities from passive seismic data. It is largely automatic and independent of a priori information. The method requires a sufficiently dense receiver network nearby the epicentre of the considered event. Using coherence analysis, we can estimate wavefront attributes for the recorded signals, tag and thereby distinguish different events and obtain an initial guess of their respective source excitation times. Since this guess may display significant errors, a refinement is usually required. Such a refinement is achieved by adding the source excitation times to the unknowns in wavefront tomography. Provided that a reasonable starting guess is available, this approach corrects large deviations in the source excitation times and jointly delivers a velocity model that is consistent with the data. This model is then used in an imaging step applying reverse time modelling to obtain an improved and probabilistic idea of the source locations based on the recorded waveform data. The presented data examples have underlined the robustness and efficiency of the workflow, delivering velocity estimations with a mean deviation of about $4\ \%$ and locations with maximum errors of about the dominant wavelength. We have obtained reliable results even from extremely noisy as well as sparsely sampled data because of the built-in data enhancement and regularisation facility.

Constructing a recursive scheme that iteratively updates the source excitation times for the tomography based on the event locations obtained from the imaging step might have strong potential. The demonstrated examples are simple in a sense that we have used explosive sources in an acoustic, isotropic medium, however, this is not a limitation inherent to the method. Other source mechanisms and additional phases may be included in further investigations. Since the theory has already been presented for 3D media and the extension of the computer codes to 3D is straight forward, a field data application is a logical next step.

ACKNOWLEDGEMENTS

The authors thank the Applied Seismic Group Hamburg and in particular Pavel Znak for fruitful and continuous discussion. This work has been supported by the sponsors of the Wave Inversion Technology (WIT) consortium and the Federal Ministry for Economic Affairs and Energy of Germany (BMWi, 03SX427B).

The second author has been supported by a research fellowship of the German Research Foundation (DFG, SCHW 1870/1-1). Matlab and especially its optimisation toolbox have been used for computations.

REFERENCES

Aki, K., Fehler, M., and Das, S. (1977). Source mechanism of volcanic tremor: Fluid-driven crack models and their application to the 1963 Kilauea eruption. *Journal of Volcanology and Geothermal Research*, 2(3):259–287.

Bauer, A., Schwarz, B., and Gajewski, D. (2017a). Quantifying diffracted and passive event location uncertainties with local wavefront measurements. In *79th EAGE Conference and Exhibition 2017*.

Bauer, A., Schwarz, B., and Gajewski, D. (2017b). Utilizing diffractions in wavefront tomography. *Geophysics*, 82(2):R65–R73.

Baykulov, M. and Gajewski, D. (2009). Prestack seismic data enhancement with partial common-reflection-surface (CRS) stack. *Geophysics*, 74(3):V49–V58.

Castle, R. J. (1994). A theory of normal moveout. *Geophysics*, 59(6):983–999.

De Boor, C. (1978). *A practical guide to splines*. Springer.

Duveneck, E. (2004). Velocity model estimation with data-derived wavefront attributes. *Geophysics*, 69(1):265–274.

Gajewski, D., Anikiev, D., Kashtan, B., Tessmer, E., and Vanelle, C. (2007). Localization of seismic events by diffraction stacking. In *77th SEG Meeting and Exposition 2007*.

Gajewski, D. and Tessmer, E. (2005). Reverse modelling for seismic event characterization. *Geophysical Journal International*, 163(1):276–284.

Grigoli, F., Cesca, S., Amoroso, O., Emolo, A., Zollo, A., and Dahm, T. (2013). Automated seismic event location by waveform coherence analysis. *Geophysical Journal International*, 196(3):1742–1753.

Hooke, R. and Jeeves, T. A. (1961). "Direct search" solution of numerical and statistical problems. *Journal of the ACM (JACM)*, 8(2):212–229.

Hubral, P. (1983). Computing true amplitude reflections in a laterally inhomogeneous earth. *Geophysics*, 48(8):1051–1062.

Ishii, M., Shearer, P. M., Houston, H., and Vidale, J. E. (2005). Extent, duration and speed of the 2004 Sumatra-Andaman earthquake imaged by the Hi-Net array. *Nature*, 435(7044):933.

Jäger, R., Mann, J., Höcht, G., and Hubral, P. (2001). Common-reflection-surface stack: Image and attributes. *Geophysics*, 66(1):97–109.

Kennett, B. L. N. and Engdahl, E. R. (1991). Traveltimes for global earthquake location and phase identification. *Geophysical Journal International*, 105(2):429–465.

Landa, E., Keydar, S., and Moser, T. J. (2010). Multifocusing revisited - Inhomogeneous media and curved interfaces. *Geophysical Prospecting*, 58(6):925–938.

Lomax, A., Virieux, J., Volant, P., and Berge-Thierry, C. (2000). Probabilistic earthquake location in 3D and layered models. In *Advances in seismic event location*, pages 101–134. Springer.

Mann, J., Jäger, R., Müller, T., Höcht, G., and Hubral, P. (1999). Common-reflection-surface stack - A real data example. *Journal of Applied Geophysics*, 42(3-4):301–318.

Maxwell, S. C. and Urbancic, T. I. (2001). The role of passive microseismic monitoring in the instrumented oil field. *The Leading Edge*, 20(6):636–639.

Mayne, W. H. (1962). Common reflection point horizontal data stacking techniques. *Geophysics*, 27(6):927–938.

Paige, C. C. and Saunders, M. A. (1982). LSQR: An algorithm for sparse linear equations and sparse least squares. *ACM Transactions on Mathematical Software (TOMS)*, 8(1):43–71.

Schleicher, J., Tygel, M., and Hubral, P. (1993). Parabolic and hyperbolic paraxial two-point traveltimes in 3D media. *Geophysical Prospecting*, 41(4):495–513.

Schwarz, B., Bauer, A., and Gajewski, D. (2016). Passive seismic source localization via common-reflection-surface attributes. *Studia Geophysica et Geodaetica*, 60(3):531–546.

Schwarz, B., Vanelle, C., Gajewski, D., and Kashtan, B. (2014). Curvatures and inhomogeneities: An improved common-reflection-surface approach. *Geophysics*, 79(5):S231–S240.

Sun, J., Xue, Z., Zhu, T., Fomel, S., and Nakata, N. (2016). Full-waveform inversion of passive seismic data for sources and velocities. In *86th SEG Meeting and Exposition 2016*.

Taner, M. T. and Koehler, F. (1969). Velocity spectra - Digital computer derivation applications of velocity functions. *Geophysics*, 34(6):859–881.

Tarantola, A. (2005). *Inverse problem theory and methods for model parameter estimation*. SIAM.

Ursin, B. (1982). Quadratic wavefront and traveltime approximations in inhomogeneous layered media with curved interfaces. *Geophysics*, 47(7):1012–1021.

Waldhauser, F. and Ellsworth, W. L. (2000). A double-difference earthquake location algorithm: Method and application to the northern Hayward fault, California. *Bulletin of the Seismological Society of America*, 90(6):1353–1368.

Wang, H. and Alkhalifah, T. (2018). Microseismic imaging using a source function independent full waveform inversion method. *Geophysical Journal International*, 214(1):46–57.

Xie, Y. and Gajewski, D. (2017). 5-D interpolation with wave-front attributes. *Geophysical Journal International*, 211(2):897–919.

Zhebel, O., Gajewski, D., and Vanelle, C. (2011). Localization of seismic events in 3D media by diffraction stacking. In *73rd EAGE Conference and Exhibition 2011*.

Znak, P., Kashtan, B., and Gajewski, D. (2018). Velocity model building by geometrical spreading focusing. In *88th SEG Meeting and Exposition 2018*.